applied sciences

MDPI

Article

Predicting the Effect of Processing Parameters on Caliber-Rolled Mg Alloys through Machine Learning

Jinyeong Yu [1], Seung Jun Oh [1], Seunghun Baek [1], Jonghyun Kim [2,*] and Taekyung Lee [1,*]

[1] School of Mechanical Engineering, Pusan National University, Busan 46241, Korea
[2] College of Materials Science and Engineering, Chongqing University, Chongqing 400044, China
* Correspondence: joindoc@cqu.edu.cn (J.K.); taeklee@pnu.edu (T.L.)

Abstract: The multi-pass caliber rolling (MPCR) of Mg alloy has attracted much attention due to its engineering and manufacturing advantages. The MPCR process induces a unique microhardness variation, which has only been predicted using a finite element analysis thus far. This study employed machine learning as an alternative method of microhardness prediction for the first time. For this purpose, two machine-learning approaches were evaluated: the artificial neural network (ANN) approach and that aided by generative adversarial networks (GANs). These approaches predicted microhardness variation in the most difficult case (i.e., after the final-pass MPCR deformation). The machine-learning approaches provided a good prediction for the center area of the cross-section, because the prediction was relatively easy due to the small deviation in microhardness. In contrast, the ANN failed to anticipate the shifted hardness variation in the side sections, leading to a low predictability. Such an issue was effectively improved by integrating the GAN with the ANN.

Keywords: magnesium; caliber rolling; hardness; machine learning; artificial neural network; generative adversarial networks

Citation: Yu, J.; Oh, S.J.; Baek, S.; Kim, J.; Lee, T. Predicting the Effect of Processing Parameters on Caliber-Rolled Mg Alloys through Machine Learning. *Appl. Sci.* **2022**, *12*, 10646. https://doi.org/10.3390/app122010646

Academic Editors: Michael Oluwatosin Bodunrin, Desmond Klenam and Japheth Obiko

Received: 30 September 2022
Accepted: 18 October 2022
Published: 21 October 2022

1. Introduction

Multi-pass caliber rolling (MPCR) is a metal-forming process used to fabricate a rod-type product. A metallic material is inserted into a "caliber" between a pair of rolls, by which it goes through redundant strains as well as shape change. Although the idea of MPCR was reported in the early 2000s [1], it gained significant attention because of the study of Kimura et al. [2] published in 2018. These authors compared the mechanical properties of Fe-0.4C-2Si-1Cr-1Mo steels subjected to either the MPCR process or a conventional method. The MPCR-processed steel presented peculiar fracture behavior resembling that of bamboo, leading to 16-fold higher impact toughness compared with conventional steel. Such a remarkable improvement was attributed to ultrafine elongated grains and nano-sized carbides fabricated by the MPCR process. The mechanical improvement by the MPCR process has attracted a large amount of attention, leading to a number of related studies using not only steels [3–6] but also nonferrous metals, such as Ti [7–10], Nb [11], and Mg alloys [12–17]. In addition, the MPCR process enables the continuous manufacturing of bulk product, while inducing either ultrafine elongated or ultrafine equiaxed grains. For example, the authors fabricated a 2 m long Mg rod with an ultrafine-grained structure using an optimized MPCR process [13]. These engineering advantages are a novelty of the MPCR process contrasted by severe plastic deformation processes.

A unique feature of the MPCR process is its strain distribution on the cross-sectional area, which varies with the type of calibers. The difference in local strain induces a heterogeneous grain structure and resultant variation in mechanical properties, particularly the Vickers microhardness [18,19]. Despite its importance, no studies have attempted to predict the microhardness variation on the MPCR cross-section using a constitutive approach for two reasons. First, these approaches (e.g., the Hall–Petch equation [20,21]) were made for

a uniform grain structure, which mean they are inapplicable to the issue of interest. Second, the size of the microhardness database is smaller than that of other mechanical properties, such as flow curves, each including thousands of data points [22]. Accordingly, all related studies [18,19,23] used finite element analysis (FEA) to predict the microhardness variation in MPCR-processed alloys.

Our research group has employed a machine-learning approach as an alternative resolution to predict the microhardness variation, because it is appropriate to solve a multivariant nonlinear problem [24]. This approach has recently proven its usefulness for other types of process and material. Khalaj et al. [25] developed a microhardness model for oxide precipitation hardened steel using machine learning, which provided good productivity with an R^2 of 0.95. Sembiring et al. [26] anticipated the microhardness values of Ni alloy subjected to ultrasonic nanocrystalline surface modification depending on the chemical composition and processing parameter. Their machine-learning model yielded an R^2 of 0.98 from 37 testing datasets. However, it should be noted that such an approach has not been verified for either MPCR or Mg alloys. Therefore, this study aimed to predict the microhardness variation in MPCR-processed AZ31 Mg alloy depending on the position as well as the processing parameter. A predictive model were constructed using an artificial neural network (ANN), one of the most frequently used machine-learning approaches, with hyperparameter optimization. Furthermore, generative adversarial networks (GANs) were validated to confirm if it could resolve the issue of a small database.

2. Materials and Methods

2.1. Experimental Procedures

Commercially extruded AZ31 Mg alloy was prepared for the present research. The chemical composition of the alloy was 3.6 wt.% Al, 1.0 wt.% Zn, 0.5 wt.% Mn, and balance Mg. This alloy exhibits a tensile yield strength of 248 MPa, compressive yield strength of 109 MPa, ultimate tensile strength of 339 MPa, and elongation to failure of 20.2% [27]. Eight cylindrical samples were machined from the single extruded alloy which were 15 mm in diameter and 175 mm in length and aligned with the extrusion direction. These samples were homogenized at 673 K for 10 h and then subjected to the MPCR process in an ambient atmosphere. The samples were soaked in a furnace at 673 K for 1 h before being inserted to the first pass of MPCR. For each deformation pass, the samples were heated for 1 min at the sample temperature, rotated 90° with the axis of extrusion, and then inserted into the next caliber. The eight samples were deformed up to the first to the eighth MPCR passes, respectively, to induce various microhardness levels and distributions.

Variations in Vickers microhardness values were obtained per MPCR deformation pass (HM-220, Mitutoyo, Kawasaki, Japan). The cross-sectional areas were mechanically polished with #1200 and #2400 emery paper to increase the data reliability. The microhardness values were measured along two directions of horizontal and vertical axes with a step size of approximately 500 μm.

The experiments yielded 1610 instances with five features: microhardness, MPCR deformation pass, and the position of measurement in three-dimensional Cartesian coordinates. Before the machine learning, all data (x) were standardized with an average (μ) and standard deviation (σ) to minimize the scale effect of each feature:

$$z = \frac{x - \mu}{\sigma} \quad (1)$$

Seventy-one instances after eight-pass MPCR deformation were designated as the test dataset. It is noted that such a designation requires extrapolation, which increases the difficulty in prediction on purpose. The remaining 1539 instances were arbitrarily divided into the train and validation datasets at a ratio of 8:2 (i.e., 1231 and 308 instances, respectively).

2.2. Finite Element Analysis

FEA was performed using commercial software ANSYS to calculate the strain distribution on the cross-sectional area subjected to eight-pass MPCR deformation (Figure 1). The workpiece consisted of a brick element to account for deformations in the element. Hexahedral meshes were generated to account for the large geometric deformations. To guarantee the element shape test, the element size was controlled for more than ten elements per unit length. The workpiece was assumed to be isotropic with a Poisson's ratio of 0.3. The same element type was applied to the pair of rolls, although they were considered as a rigid body. The friction coefficient was set to 0.3 assuming the dry contact, which was a nominal value to maintain the stick condition between the workpiece and the roll during the compression as well as the slip condition. It provided better stability for the solution convergence, since a slip motion was allowed right before and after the loading.

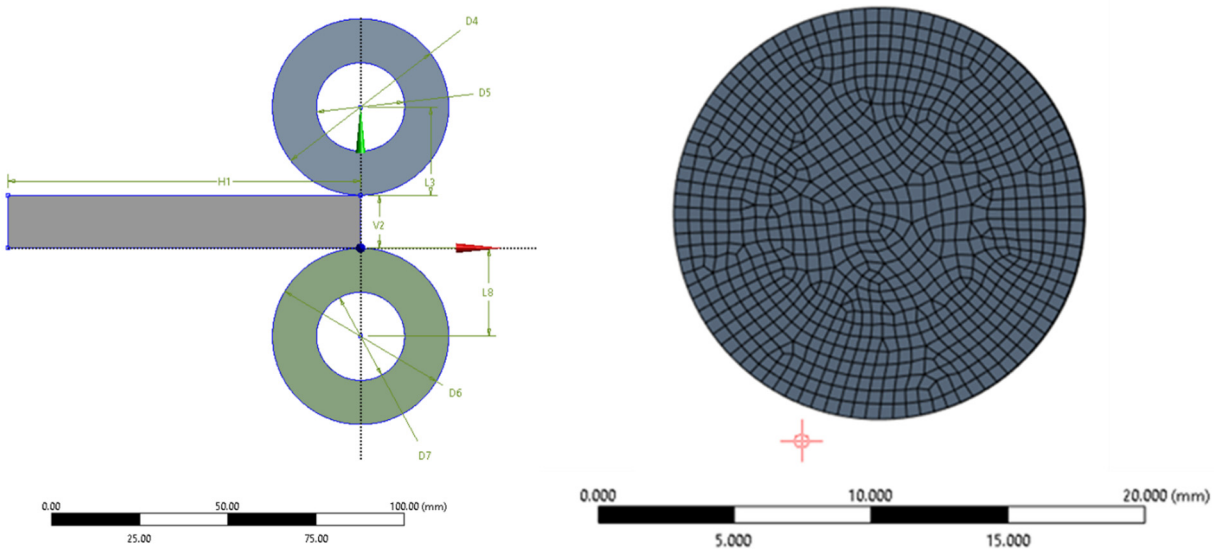

Figure 1. Scheme of the finite element model used in this study and meshes for the cross-section.

2.3. Machine Learning

An ANN can be constructed with hidden layers as well as input and output layers. The numbers of hidden layers and units are determined by the researcher, which directly affects the prediction of the performance of the ANN model. In this work, these hyperparameters were optimized using an algorithm called 'hyperband' [28] in the range of 1–10 hidden layers and 4–32 hidden units per layer. The optimum ANN architecture for this study consisted of 224, 200, 192, 72, 184, 72, 152, and 176 units in the first to eighth hidden layers, respectively. In addition, the learning rate was also optimized using the same method between 10^{-5} and 10^{-3}, for which the hyperband yielded an optimum value of $10^{-3.865}$. The LeakyReLU [29] and mean square error were chosen as the activation and loss functions, respectively. The adaptive moment estimation [30] was employed for the stochastic optimization.

The GAN [31] generated fake data similar to the genuine ones using two competing functions called a discriminator and generator. Both functions used a multilayer perceptron model similar to an ANN, which consisted of two hidden layers. The size of latent space was determined as 1×64 by trial and error. The discriminator had 128 hidden units, while adopting the LeakyReLU and sigmoid for the activation functions. The generator required more complex architecture than the discriminator as it generated fake data from the noises. Accordingly, 256 hidden units were allocated to the generator, which doubled those of the discriminator. The generator also used the LeakyReLU for the activation function. Binary cross entropy was employed as the loss function for both models. Only the training dataset was provided for the learning of the GAN model at a rate of 3×10^{-4}

for 5000 epochs. The mini-batch method was adopted to make the machine learning stable and robust through iterations. The batch number was set to be 41, which was an aliquot part of 1230 instances; note that one of 1231 instances was arbitrarily excluded to avoid the overfitting of the last batch. As a result, the training dataset doubled to 2462 instances through the GAN approach. The architecture of the final model, GAN-aided ANN, is presented in illustration (Figure 2).

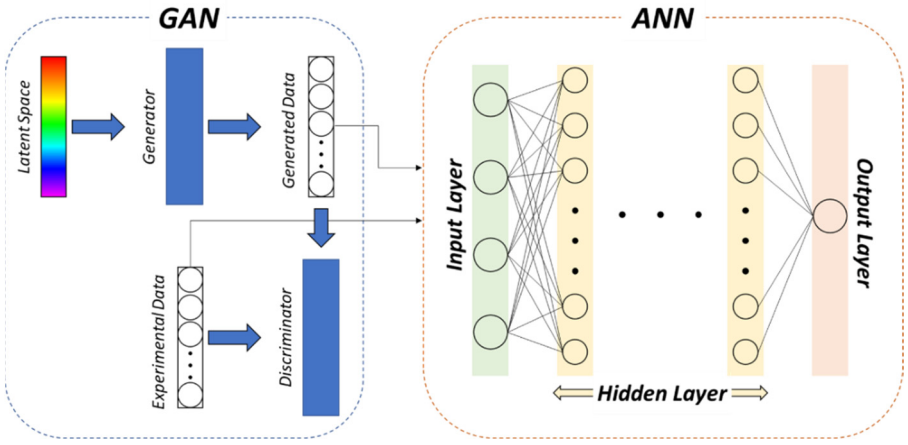

Figure 2. Graphical scheme of GAN-aided ANN model developed in the present study.

3. Results and Discussion

Table 1 summarizes the side length of caliber cross-section (s) measured by a micrometer, accumulated reduction in area (r), and equivalent strain (ε_{eq}) per MPCR deformation pass. The relation between the latter parameters is expressed as follows:

$$\varepsilon_{eq} = -\ln\left(1 - \frac{r}{100}\right) \quad (2)$$

Table 1. ε_{eq} and shape factors for its calculation for each deformation pass of MPCR process.

Pass †	0	1	2	3	4	5	6	7	8
s **(mm)**	5.30	4.91	4.56	4.17	3.89	3.50	3.29	3.04	2.79
r **(%)**	0	13.6	26.6	37.7	46.4	56.8	61.8	67.5	72.4
ε_{eq}	0	0.15	0.31	0.47	0.62	0.84	0.96	1.12	1.29

† The number of applied MPCR passes.

Increasing the number of MPCR passes imposed an increasing amount of plastic deformation, leading to the positive correlation between the ε_{eq} value and pass number. However, these calculations are insufficient to describe the precise trends of plastic deformation for two reasons. First, the results assume the uniform distribution of strains on the cross-sectional area, which is not applicable to the present case. Complex three-dimensional stress states induced by the MPCR process caused a significant difference in deformation behavior [32]. Second, the actual strain is remarkably higher than the theoretical ε_{eq} value as the latter cannot consider the redundant strain [17]. Such a disparity was confirmed in various materials including both steels [18,32] and nonferrous alloys [23,33].

FEA provided deeper insight into the two drawbacks of theoretical calculation mentioned above (Figure 3). The FEA-based ε_{eq} values were remarkably higher than the theoretical value calculated using Equation (2) (1.29), as aforementioned. Furthermore, the eight-pass MPCR process gave rise to a significant inhomogeneity of ε_{eq} values on the cross-section. The ε_{eq} value for the corner sections (2.08) was significantly higher than that for the center (1.78). This type of ε_{eq} distribution arose from the MPCR process, rather than from the material, because the similar distribution was reported from 0.15C–0.3Si–1.5Mn–0.01P–0.002S steel subjected to the MPCR process [18]. Specifically, diamond calibers led to

the given ε_{eq} distribution [18,23]. The FEA also demonstrated the significant local strain at the interface between the rod surface and roll, as shown in Figure 3b. Conversely, oval and circular calibers accumulate strain on the center, leading to different ε_{eq} distribution [32,33].

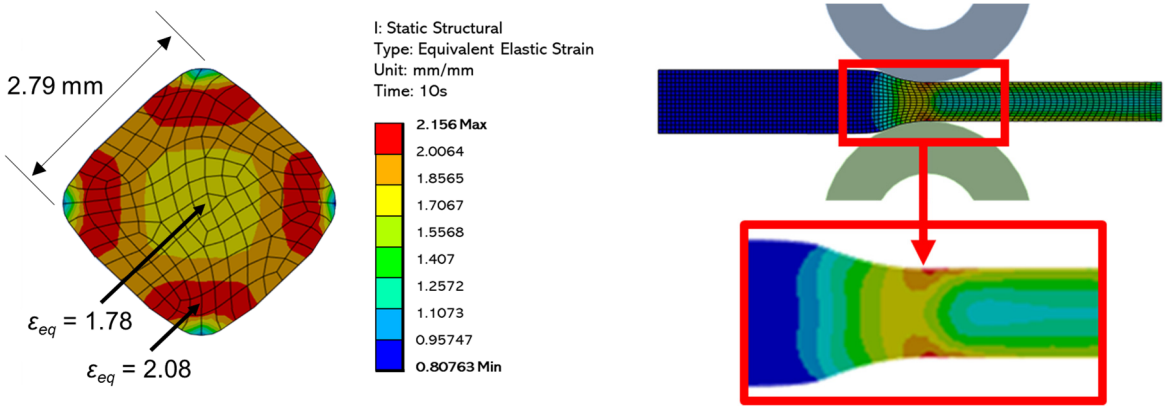

Figure 3. FEA contour maps of ε_{eq} for AZ31 Mg alloy subjected to the eight-pass MPCR deformation: (**a**) on the cross-section and (**b**) on the lateral view.

Vickers microhardness values were measured along the transverse direction on the cross-sectional areas (Figure 4). The hardness increased with increasing amounts of MPCR deformation from the first to fourth pass (Stage I). It became steady at ~83 HV from the fourth to sixth pass (Stage II), and then increased again up to the eighth MPCR pass (Stage III). The suppressed hardness increment between the fourth and sixth passes can be understood using microstructural evolution. Dynamic recrystallization occurs during the MPCR process for Mg alloy, which consists of (i) the formation of fine arrays surrounded by low-angle grain boundaries and (ii) the conversion of them into recrystallized grains with high-angle grain boundaries [13]. Stages I and II correspond to these steps, respectively. The first dynamic recrystallization was completed in Stage II, leading to the steady state of microhardness. Further straining in Stage III induced the second dynamic recrystallization including the subgrain refinement, and thus increased the hardness again. Inoue et al. [23] confirmed the microstructural evolution of MPCR-processed Mg alloy based on these stages.

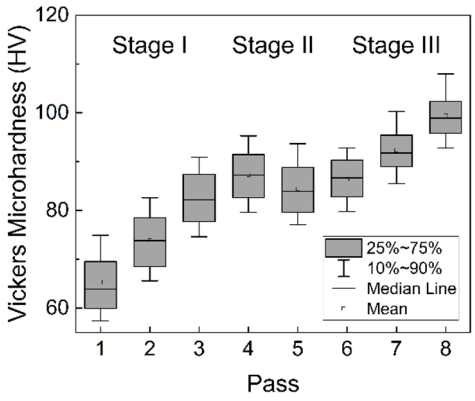

Figure 4. Variation in Vickers microhardness values depending on the number of applied MPCR deformation passes.

The expected and predicted microhardness values were arranged along the distance across the cross-section (Figure 5). The experimental data exhibited V-shaped variation, where the center exhibited low hardness and the two edges showed high values. These results were rationalized by the aforementioned inhomogeneity of ε_{eq} values, as shown in

Figure 3a. Compared with the FEA results as well as the literature [18,23,32,33], the actual hardness distribution was shifted towards the regime of higher distances. The hardness at the left edge of the cross-section (115 HV at a distance of 0 mm) was higher than that of the right edge (110 HV at a distance of 7.5 mm). In addition, the lowest hardness was confirmed not at the center but at the point pushed over towards the right edge (89 HV at a distance of 6 mm). Such a result arose from the imperfect rolling including the imbalance of lubrication and the disparity in rotation speed between the two rolls. This is also supported by the bent rod after the eight-pass MPCR deformation. The significant shear on the rod surface, as shown in Figure 3b, barely changed in spite of the imperfect rolling conditions. Therefore, the V-shaped variation in microhardness was maintained with the slight movement of the center.

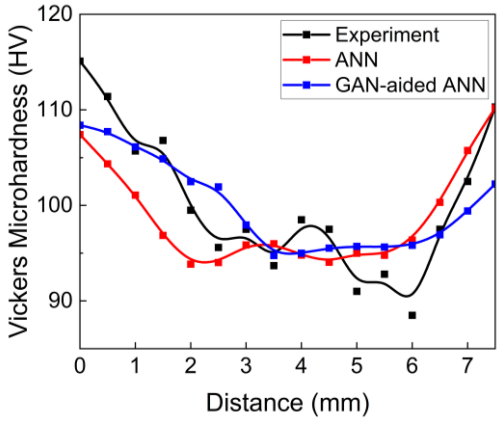

Figure 5. Line profile of Vickers microhardness values along the distance across the cross-section subjected to the eight-pass MPCR deformation. The data predicted by ANN and GAN-aided ANN approaches were also presented in the same format.

The predictability of machine learning was evaluated in three groups: the center, the left section, and the right section (Figure 6). The left and right sections indicate 25% distance from each edge. As shown in Figure 6a, the data were shown in the form of the root mean squared error (RMSE) for a quantitative analysis, expressed as:

$$\mathrm{RMSE} = \sqrt{\sum_{i=1}^{n} \frac{(y_i - \hat{y}_i)^2}{n}} \tag{3}$$

where n is the total number of data, y_i is the genuine datum, and $\hat{y}_i$ is the predicted one. The ANN approach provided good predictability for the center area with a low RMSE of 3.03 HV. Integrating the GAN hardly enhanced the predictability with an RMSE of 2.98 HV. The ANN prediction for microhardness in the side sections was more difficult, as characterized by a significant increase in the RMSE to 7.33 HV for the left and 3.18 HV for the right. It should be noted that the GAN-aided ANN remarkably improved the predictability for this case. The RMSE was more than halved to 3.18 HV for the left side, although it was slightly increased to 4.76 HV for the right. Comparing the error rates of two models also provided a consistent conclusion, as shown in Figure 6b. The GAN-aided ANN model showed similar or lower error rates compared with the ANN in all experimental positions, except for the points at 2.5 and 7.5 mm. In particular, the GAN integration remarkably reduced the error rates from 10% to 5% at maximum in the left section.

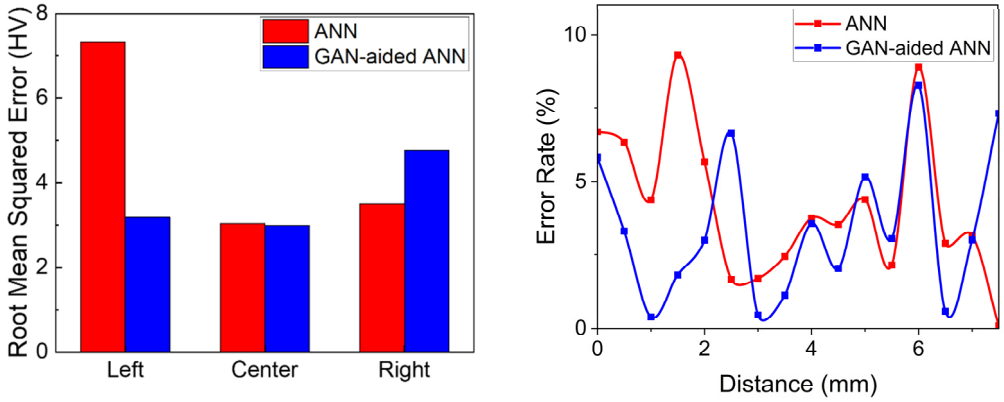

(**a**) (**b**)

Figure 6. Comparing predictability for Vickers microhardness between ANN and GAN-aided ANN approaches: (**a**) RMSE values for the left section (0–2 mm in distance from the left edge), center (2–5.5 mm), and right section (5.5–7.5 mm); (**b**) the variation in error rates per datum as a function of distance.

The different effect of the GAN integration in relation to cross-sectional position can be understood in light of the shifted hardness distribution. The center area had a uniform distribution of hardness ranging from 91 to 99 HV. This condition was easy to predict for both approaches, resulting in the similarly low RMSE values. In contrast, the side sections were significantly more difficult to predict due to the shifted hardness distribution as well as the large hardness variation from 89 to 115 HV. The ANN prediction was insufficient for these areas, as clearly seen by the symmetric hardness distribution in Figure 5. However, integrating the GAN with the ANN plotted the shifted distribution towards the regime of higher distances reflecting the trends of experimental data. This resulted in the considerable reduction in RMSE by integrating the GAN. The improved predictability stemmed from the doubled amount of microhardness samples generated by the GAN approach. The slight increase in RMSE in the right side was attributed to the overfitting for the hardness shift towards the higher distance. In conclusion, integrating the GAN with the ANN can improve the predictability of hardness distribution that is even distorted by the imperfect manufacturing condition.

4. Conclusions

There have been no studies that exploit machine learning to model the mechanical properties of MPCR-processed Mg alloys. This study employed two machine-learning approaches (i.e., the ANN and GAN-aided ANN) to predict the effect of the MPCR processing parameters on the microhardness of AZ31 Mg alloy. The ANN approach was prepared by hyperparameter optimization. A constitutive approach failed to provide precise equivalent strains as it disregarded the complex stress states and redundant strains of MPCR deformation. FEA suggested the radical V-shaped distribution of strains induced by diamond calibers, resulting in the similar distribution of microhardness values. The center of V-shaped distribution was shifted towards the higher distance owing to the imperfect manufacturing, thereby increasing the predictive difficulty for the present study. The ANN provided a good prediction for the center area where the microhardness values showed the uniform distribution with the small deviation (±5 HV). Integrating GAN gave rise to the negligible improvement in prediction, since the ANN itself was sufficient to predict this regime. However, the predictive difficulty exceedingly increased in the side sections due to the increased deviation (±13 HV) and the shifted center of V-shaped hardness variation. The ANN plotted the symmetric hardness variation, suggesting that it failed to provide a useful prediction for this regime. In contrast, the GAN-aided ANN successfully anticipated the shift with the reduced RMSE compared with the ANN approach. Thus, integrating the GAN with the ANN can improve the predictability of hardness distribution

even when it is distorted by imperfect manufacturing conditions. The applicability of the GAN-aided ANN approach needs to be confirmed for other mechanical properties, such as mechanical strength, ductility, fatigue limit, and toughness.

Author Contributions: Conceptualization, T.L.; methodology, J.Y., S.B. and T.L.; software, J.Y. and S.B.; investigation, S.J.O.; resources, J.K. and T.L.; writing—original draft preparation, J.Y., S.B., J.K. and T.L.; writing—review and editing, T.L.; visualization, J.Y., S.B. and T.L.; supervision, T.L.; project administration, T.L. All authors have read and agreed to the published version of the manuscript.

Funding: This research was supported by 2021 BK21 FOUR Program of Pusan National University.

Data Availability Statement: The data presented in this study are available on request.

Conflicts of Interest: The authors declare no conflict of interest.

References

1. Komori, K. Simulation of deformation and temperature in caliber rolling: Effect of finite-element mesh in cross-section. *J. Mater. Process. Technol.* **2003**, *143–144*, 367–372. [CrossRef]
2. Kimura, Y.; Inoue, T.; Yin, F.; Tsuzaki, K. Inverse Temperature Dependence of Toughness in an Ultrafine Grain-Structure Steel. *Science* **2008**, *320*, 1057–1060. [CrossRef]
3. Inoue, T.; Yin, F.; Kimura, Y.; Tsuzaki, K.; Ochiai, S. Delamination Effect on Impact Properties of Ultrafine-Grained Low-Carbon Steel Processed by Warm Caliber Rolling. *Metall. Mater. Trans. A* **2010**, *41*, 341–355. [CrossRef]
4. Lee, T.; Park, C.H.; Lee, D.-L.; Lee, C.S. Enhancing tensile properties of ultrafine-grained medium-carbon steel utilizing fine carbides. *Mater. Sci. Eng. A* **2011**, *528*, 6558–6564. [CrossRef]
5. Kimura, Y.; Inoue, T.; Akiyama, E. Warm tempforming effect on the hydrogen embrittlement of 1.8-GPa-class ultra-high-strength low-alloy steel. *Mater. Sci. Eng. A* **2017**, *703*, 503–512. [CrossRef]
6. Hwang, J.K.; Kim, S.J. Effect of reduction in area per pass on strain distribution and microstructure during caliber rolling in twinning-induced plasticity steel. *J. Iron Steel Res. Int.* **2019**, *27*, 62–74. [CrossRef]
7. Krállics, G.; Gubicza, J.; Bezi, Z.; Barkai, I. Manufacturing of ultrafine-grained titanium by caliber rolling in the laboratory and in industry. *J. Mater. Process. Technol.* **2014**, *214*, 1307–1315. [CrossRef]
8. Babu, S.M.J.; Murty, S.V.S.N.; Prabhu, N.; Kashyap, B.P. An evidence of pseudo-elasticity in a caliber rolled Ti6Al4V alloy and its effect on tension-compression flow asymmetry. *Mater. Sci. Eng. A* **2019**, *754*, 650–658. [CrossRef]
9. Topolski, K.; Garbacz, H. Manufacturing of nanostructured titanium Grade2 using caliber rolling. *Mater. Sci. Eng. A* **2019**, *739*, 277–288. [CrossRef]
10. Lee, T.; Lee, S.; Kim, I.-S.; Moon, Y.H.; Kim, H.S.; Park, C.H. Breaking the limit of Young's modulus in low-cost Ti–Nb–Zr alloy for biomedical implant applications. *J. Alloys Compd.* **2020**, *828*, 154401. [CrossRef]
11. Lee, J.; Jeong, H. Effect of Rolling Speed on Microstructural and Microtextural Evolution of Nb Tubes during Caliber-Rolling Process. *Metals* **2019**, *9*, 500. [CrossRef]
12. Tripathi, A.; Murty, S.V.S.N.; Narayanan, P.R. Microstructure and texture evolution in AZ31 magnesium alloy during caliber rolling at different temperatures. *J. Magnes. Alloys* **2017**, *5*, 340–347. [CrossRef]
13. Lee, T.; Kwak, B.J.; Kong, T.; Lee, J.H.; Lee, S.W.; Park, S.H. Enhanced yield symmetry and strength-ductility balance of caliber-rolled Mg–6Zn-0.5Zr with ultrafine-grained structure and bulk dimension. *J. Alloys Compd.* **2019**, *803*, 434–441. [CrossRef]
14. Liu, N.; Chen, L.; Fu, Y.; Zhang, Y.; Tan, T.; Yin, F.; Liang, C. Interfacial characteristic of multi-pass caliber-rolled Mg/Al compound castings. *J. Mater. Process. Technol.* **2019**, *267*, 196–204. [CrossRef]
15. Somekawa, H.; Basha, D.A.; Singh, A. Change in dominant deformation mechanism of Mg alloy via grain boundary control. *Mater. Sci. Eng. A* **2019**, *746*, 162–166. [CrossRef]
16. Kwak, B.J.; Park, S.H.; Moon, Y.H.; Lee, J.H.; Lee, T. Plastic anisotropy of multi-pass caliber-rolled Mg alloy with split texture distribution. *Mater. Sci. Eng. A* **2020**, *788*, 139496. [CrossRef]
17. Kong, T.; Kwak, B.J.; Kim, J.; Lee, J.H.; Park, S.H.; Kim, J.H.; Moon, Y.H.; Yoon, H.S.; Lee, T. Tailoring strength-ductility balance of caliber-rolled AZ31 Mg alloy through subsequent annealing. *J. Magnes. Alloys* **2020**, *8*, 163–171. [CrossRef]
18. Inoue, T.; Yin, F.; Kimura, Y. Strain distribution and microstructural evolution in multi-pass warm caliber rolling. *Mater. Sci. Eng. A* **2007**, *466*, 114–122. [CrossRef]
19. Hwang, J.-K.; Yi, I.-C.; Son, I.-H.; Yoo, J.-Y.; Kim, B.; Zargaran, A.; Kim, N.J. Microstructural evolution and deformation behavior of twinning-induced plasticity (TWIP) steel during wire drawing. *Mater. Sci. Eng. A* **2015**, *644*, 41–52. [CrossRef]
20. Kim, J.G.; Seol, J.B.; Park, J.M.; Sung, H.; Park, S.H.; Kim, H.S. Effects of Cell Network Structure on the Strength of Additively Manufactured Stainless Steels. *Met. Mater. Int.* **2021**, *27*, 2614–2622. [CrossRef]
21. Lee, Y.; Kim, E.S.; Park, S.; Park, J.M.; Seol, J.B.; Kim, H.S.; Lee, T.; Sung, H.; Kim, J.G. Effects of Laser Power on the Microstructure Evolution and Mechanical Properties of Ti–6Al–4V Alloy Manufactured by Direct Energy Deposition. *Met. Mater. Int.* **2022**, *28*, 197–204. [CrossRef]

22. Lee, T.; Kwak, B.J.; Yu, J.; Lee, J.H.; Noh, Y.; Moon, Y.H. Deep-learning approach to predict a severe plastic anisotropy of caliber-rolled Mg alloy. *Mater. Lett.* **2020**, *269*, 127652. [CrossRef]
23. Inoue, T.; Somekawa, H.; Mukai, T. Hardness Variation and Strain Distribution in Magnesium Alloy AZ31 Processed by Multi-pass Caliber Rolling. *Adv. Eng. Mater.* **2009**, *11*, 654–658. [CrossRef]
24. Yu, J.; Lee, M.; Moon, Y.H.; Noh, Y.; Lee, T. Prediction of Electropulse-Induced Nonlinear Temperature Variation of Mg Alloy Based on Machine Learning. *Korean J. Met. Mater.* **2020**, *58*, 413–422. [CrossRef]
25. Khalaj, O.; Ghobadi, M.; Zarezadeh, A.; Saebnoori, E.; Jirková, H.; Chocholaty, O.; Svoboda, J. Potential role of machine learning techniques for modeling the hardness of OPH steels. *Mater. Today Commun.* **2021**, *26*, 101806. [CrossRef]
26. Sembiring, J.P.B.A.; Amanov, A.; Pyun, Y.S. Artificial neural network-based prediction model of residual stress and hardness of nickel-based alloys for UNSM parameters optimization. *Mater. Today Commun.* **2020**, *25*, 101391. [CrossRef]
27. Kim, S.-H.; Bae, S.W.; Lee, S.W.; Moon, B.G.; Kim, H.S.; Kim, Y.M.; Yoon, J.; Park, S.H. Microstructural evolution and improvement in mechanical properties of extruded AZ31 alloy by combined addition of Ca and Y. *Mater. Sci. Eng. A* **2018**, *725*, 309–318. [CrossRef]
28. Li, L.; Jamieson, K.; DeSalvo, G.; Rostamizadeh, A.; Talwalkar, A. Hyperband: A novel bandit-based approach to hyperparameter optimization. *J. Mach. Learn. Res.* **2018**, *18*, 1–52.
29. He, K.; Zhang, X.; Ren, S.; Sun, J. Delving deep into rectifiers: Surpassing human-level performance on imagenet classification. In Proceedings of the IEEE International Conference on Computer Vision, Santiago, Chile, 7–13 December 2015.
30. Kingma, D.P.; Ba, J.L. Adam: A method for stochastic optimization. In Proceedings of the 3rd International Conference on Learning Representations, ICLR 2015—Conference Track Proceedings, San Diego, CA, USA, 7–9 May 2015.
31. Goodfellow, I.; Pouget-Abadie, J.; Mirza, M.; Xu, B.; Warde-Farley, D.; Ozair, S.; Courville, A.; Bengio, Y. Generative Adversarial Nets. In Proceedings of the Advances in Neural Information Processing Systems, Montreal, QC, Canada, 8–13 December 2014.
32. Hwang, J.-K. Effects of caliber rolling on microstructure and mechanical properties in twinning-induced plasticity (TWIP) steel. *Mater. Sci. Eng. A* **2018**, *711*, 156–164. [CrossRef]
33. Lee, T.; Park, K.-T.T.; Lee, D.J.; Jeong, J.; Oh, S.H.; Kim, H.S.; Park, C.H.; Lee, C.S. Microstructural evolution and strain-hardening behavior of multi-pass caliber-rolled Ti-13Nb-13Zr. *Mater. Sci. Eng. A* **2015**, *648*, 359–366. [CrossRef]